Polarimetric Radar Cross-Sections of Pedestrians at Automotive Radar Frequencies

by

Yoshana Deep

Under the supervision of
Dr. Shobha Sundar Ram

Department of Electronics and Communication
Engineering
Indraprastha Institute of Information technology, Delhi
June, 2019

Polarimetric Radar Cross-Sections of Pedestrians at Automotive Radar Frequencies

by

Yoshana Deep

A thesis submitted
in partial fulfillment for the degree of
Master of Technology

to

Indraprastha Institute of Information technology, Delhi
June, 2019

Certificate

This is to certify that the thesis titled "*Polarimetric Radar Cross-Sections of Pedestrians at Automotive Radar Frequencies*" being submitted by *Yoshana Deep (MT17128)* to the Indraprastha Institute of Information Technology Delhi, for the award of the Master of Technology, is an original research work carried out by her under my supervision. In my opinion, the thesis has reached the standards fulfilling the requirements of the regulations relating to the degree.

The results contained in this thesis have not been submitted in part or full to any other university or institute for the award of any degree.

Date: _____

Dr. Shobha Sundar Ram

Department of electronics and communication engineering

Indraprastha Institute of Information Technology Delhi

New Delhi 110 020

Dedicated to my beloved family and friends . . .

Acknowledgement

<div align="right">
Yoshana Deep

Indraprastha Institute of Information Technology, Delhi

June, 2019
</div>

Abstract

Simulation of radar cross-sections (RCS) of pedestrians at automotive radar frequencies forms a key tool for software verification test beds for advanced driver assistance systems. Two commonly used simulation methods are: the computationally simple scattering center model of dynamic humans; and the shooting and bouncing ray technique based on geometric optics. The latter technique is more accurate but due to its computational complexity, it is usually used only for modeling scattered returns of still human poses. In this work, we combine the two methods in a linear regression framework to accurately estimate the scattering coefficients or reflectivies of the point scatterer model which we subsequently use to simulate range-time, Doppler-time and range-Doppler radar signatures for a realistic automotive radar signal model. The simulated signatures show a normalized mean square error below 10% and a structural similarity above 81% with respect to measurement results generated with an automotive radar at 77 GHz.

Contents

List of Tables

List of Figures

Chapter 1

Introduction

1.1 Motivation

Pedestrians - especially children, senior citizens and those with disabilities - are among the most vulnerable road users. Anywhere from 12% to 38% of the road fatalities occur to pedestrians [1]. Recently, there has been significant research focus on developing advanced driver assistance systems (ADAS) for improving driving conditions and reducing road fatalities. Pedestrian detection, one of the key objectives of ADAS, has been researched with both automotive cameras [2, 3] and radars [4, 5]. Camera images offer key features - in the form of shapes, sizes and texture cues - for enabling automatic detection and recognition. However, the performance of the camera is affected by light and visibility conditions. Automotive radars, unlike cameras, can operate continuously, under low visibility conditions and, in some cases, in non-line-of-sight conditions as well. Most importantly, the swinging motions of a pedestrian's arms and legs, while walking, give rise to distinctive Doppler radar signatures [6–13]. These micro-Doppler signals are different from those generated by other dynamic bodies on the road such as bicycles and cars and hence can be used for automatic target recognition [6, 14–19].

The performance of these algorithms rely on the availability of large training databases gathered in a variety of scenarios. They must comprise of data from pedestrians of different ages, heights and girth; performing different activities and moving at different orientations with respect to the radar. There are two methods of generating the training data. One method is to collect the data from real pedestrians using actual automotive radar sensors. The advantage is that the training data is real and can be gathered both in laboratory conditions and during test drives. However, the disad-

vantage is that the database must be updated based on hardware modifications to the sensor or due to software changes in the signal processing. Second, the data may be corrupted by the presence of clutter from the local environment (both static and dynamic) and limitations of the sensor. Labelling of radar measurement data gathered over long test drives also requires painstaking efforts. Finally, pedestrians are dielectric bodies of much smaller RCS than other road targets and are unpredictable in terms of motion and posture. The alternative is to simulate the radar signatures [20]. The advantage is that the simulated radar signatures can be rapidly generated for a variety of sensor parameters and target scenarios. Also, the simulations can be easily integrated with the radar test bed and signal processing platforms for rapid prototyping and validations. Finally, since the simulated data may be made free of channel artifacts such as clutter, the simulation results may facilitate identifying cause and effect of the underlying radar phenomenology.

1.2   Literature review

Simulations of radar micro-Doppler signatures have been extensively researched over the last decade [20–23]. The methods have included simple pendulum models of the human motions [24, 25]; analytical models of walking motion derived from biomechanical experiments [26]; and computer animation models for describing more complex human motions [27–30]. The motion models are subsequently combined with electromagnetic models of radar scattering off humans. *Full wave electromagnetic solvers* yield very accurate predictions of radar cross-sections (RCS). However, they are not used for modeling humans due to the considerable computational complexity (in terms of time and memory) in modeling three-dimensional spatially large dielectric bodies at automotive radar frequencies (24 GHz and 77 GHz). Further, humans are dynamic and have a distinct pose and posture during each instant of any motion such as walking. A slightly less computationally expensive alternative is based on *shooting and bouncing rays and geometric optics* and has been used for predicting the RCS of still humans at X-band and Ku-band frequencies [31–33]. However, the technique still remains computationally expensive and cannot be used

to generate radar data at the rate of pulse repetition frequencies typically used in automotive radars. Hence, ray tracing results cannot be directly used for generating radar signatures - such as high range-resolution profiles or Doppler-time spectrograms of humans - which provide key information for automatic target recognition. A third technique based on the *point scattering center model* has been widely adopted for obtaining radar signatures of humans due to its low computational complexity [20, 34]. Here the human is modelled as an extended point target with multiple point scatterers. The scattering coefficient of each of these point scatterers is determined from an approximated analytical expression for RCS of a primitive shape resembling the human body part corresponding to the point scatterer. The time-varying positions of the point scatterers are obtained from computer animation data. The resulting radar signatures have shown excellent correlation in terms of their micro-Doppler features to the signatures derived from real measurement data. However, the method is very inaccurate in estimating the RCS magnitude due to the approximate nature of the primitive based model and because the model does not include the effects of shadowing and multipath interactions between the different body parts. However, the accurate estimation of RCS is important for the implementation of radar detectors for generating the receiver operating curves.

1.3   Objective

The objective of the proposed work is to simulate the radar scattered signal of dynamic humans in order to generate radar signatures such as range-time, Doppler-time and range-Doppler ambiguity plots, with accurate reflectivities of scattering center coefficients. Direct simulation of RCS of humans at radar sampling frequencies using electromagnetic solvers is impractical due to its computational complexity. In our method, we rely on the availability of MoCap data of a dynamic human at video frame rate to generate RCS using electromagnetic ray tracing.

1.4 Proposed methodology

In this work, we propose a method for accurately predicting the RCS of pedestrians by combining electromagnetic ray tracing with the point scatterer model. Highly accurate estimates of RCS of the human are generated at video frame rate using the ray tracing technique. The reflectivities of the point scatterer human model are then estimated from the ray tracing RCS values using linear regression. These reflectivities are subsequently integrated with the scattering center model to generate the RCS at high radar sampling frequencies. Our method is founded on the assumption that since humans are slow moving targets, their scattering coefficients fluctuate slowly across multiple radar coherent processing intervals while the positions of the point scatterers change rapidly across multiple pulse repetition intervals. The proposed method, thereby, combines the advantages of high accuracy of ray tracing with the computational performance of scattering center modeling. We derive three types of radar signatures - high range-resolution profile, Doppler-time spectrogram and range-Doppler ambiguity diagram from the simulated data. We compare the signatures with similar signatures derived from measurement radar data at 77 GHz. Our results show a low normalized mean square error (below 10%) and high structural similarity (above 81%) between the measured and simulated radar signatures. We also present calibrated monostatic and bistatic RCS of humans at multiple aspect angles, multiple polarizations and for two automotive radar frequencies (24 GHz and 77 GHz).

1.5 Thesis outline

The thesis is organized as follows:

Chapter 2: In this chapter, we provide a brief description of the fairly standard shooting and bouncing ray technique for RCS estimation. This chapter indicates the flow of modelling motion capture data to target rendered into small triangular facets. The RCS is calculated for different polarizations, aspect angles and carrier frequency.

4

Chapter 3: This chapter presents our proposed method to use the ray tracing results to estimate scattering center coefficients which are subsequently used in a point scatterer model to generate scattered signals at suitable radar sampling frequencies. Here, we detail the radar signal model in the from of received signal in terms of slow time and fast time axes. In the later part, we discuss the generation of three radar signatures viz. range-time, Doppler-time and range-Doppler ambiguity plots. The algorithm 1 summarizes the simulation methodology.

Chapter 4: In this chapter, we present and analyze the experimental results of our simulations discussed in above chapters. First, we describe the experimental set up for jointly collecting radar measurement data and motion capture (MoCap) data. Next, we present RCS obtained from electromagnetic ray tracing for different polarizations. Finally, we present the simulated radar signatures of a pedestrian and provide the qualitative (Sec. 4.2) and quantitative (Sec. 4.3) comparison with measurement results.

Notation: We use the following conventions in our notations. Scalar variables are written with small letters; vectors are denoted with overhead arrows; and matrices are written with bold face capital letters.

Chapter 2

Radar scattering simulation using electromagnetic ray tracing

In this chapter, we detail the methodology to simulate the radar returns from a complex non-rigid human using the physics of ray optics and electromagnetic theory. To simulate the dynamic human motion, computer animation data from motion capture technologies are exploited. This returns the model of target for each frame of motion in the form of stick figure. We begin with a stick figure model of a human motion obtained from MoCap technology as shown in Fig. 2.1.
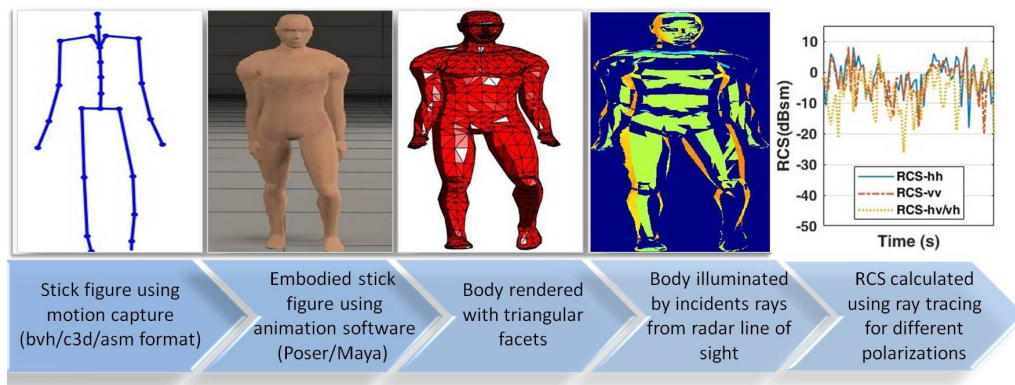
Figure 2.1: Motion capture (MoCap) data in stick figure format is embodied using animation software like Poser/Maya. Then the body is rendered with triangular facets. Radar cross-section is calculated using electromagnetic ray tracing for different polarizations.

Each frame of MoCap data is exported to an animation software, such as Poser Pro from Smith Micro Software [29], where the stick figure is embodied using one of the in-built libraries of an anatomically accurate human body. The human body is then rendered into a three-dimensional poly-mesh figure composed of Q triangular facets of suitable resolution [35]. The resulting poly-mesh data are used for further

processing.

Our objective is to estimate the RCS at f_c carrier frequency using the shooting and bouncing ray technique described in [36]. It is a very accurate but computationally extensive method to simulate the radar scattering from spatially large non-rigid targets incorporating the effects of dielectric constants of target and different polarization. In the following sections, we will briefly describe how we have applied the technique for modeling the RCS of humans. We consider a human standing on an $x - y$ ground plane with the height along the positive z axis.

2.1   Illuminating rays

We simulate a bunch of parallel rays along the radar line-of-sight, $\hat{\phi}^i$ (incident azimuth angle with respect to positive x axis), emanating from two-dimensional grid points on an illumination plane Ω_I as shown in Fig. 2.2. The rays are uniformly spaced $\frac{\lambda}{10}$ apart where λ is the wavelength, and are incident upon the poly-mesh human in the radar's far-field. Ω_I spans the size of the human along the three axes.
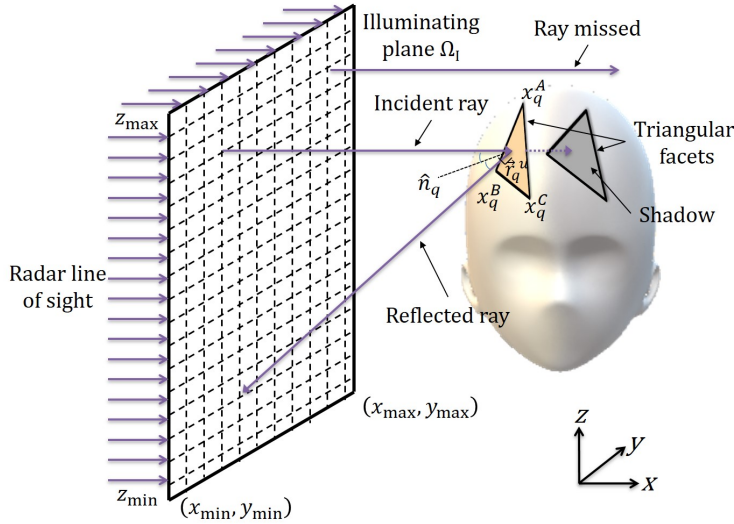
Figure 2.2: Parallel rays, along radar line-of-sight ($\hat{\phi}^i$), emanate from two dimensional grid points uniformly spaced $\frac{\lambda}{10}$ apart on an illumination plane Ω_I. An incident ray that intersects q^{th} triangular facet on human body with normal $\hat{n}^q$ gives rise to reflected ray. When an incident ray intersects more than one facet, the nearest triangular facet is assumed to be illuminated while the remaining are considered to be shadowed.

The associated electric field with each ray is

$$\vec{E}^i(\vec{r}) = \left((-\sin\phi^i \hat{x} + \cos\phi^i \hat{y}) E^{i,h} + \hat{z} E^{i,v} \right) e^{-jk\hat{\phi}^i \cdot \vec{r}}, \tag{2.1}$$

where $k = \frac{2\pi}{\lambda}$ is the propagation constant; $E^{i,h}$ and $E^{i,v}$ are the horizontal and vertical polarization components respectively and assumed to be unity; and $\vec{r}$ is the position vector of the field.

2.2   Ray - Surface intersections

We find the intersection point, $\vec{r}_q^u = [x_q^u, y_q^u, z_q^u]$, between a uth ray and a qth triangular facet with vertices, $\vec{x}_q^A, \vec{x}_q^B$ and $\vec{x}_q^C$, on the human body using

$$\begin{aligned} x_q^u &= x^u + q\cos\phi^i \\ y_q^u &= y^u + q\sin\phi^i \\ z_q^u &= z^u, \end{aligned} \tag{2.2}$$

where $\vec{r}^u = [x^u, y^u, z^u]$ is the originating point of the uth ray on Ω_I. The vertices of the triangle are along the anti clock-wise direction. Since $\vec{r}_q^u$ also lies on the plane of the triangle,

$$\hat{n}_q \cdot \left(\vec{r}_q^u - \vec{x}_q^A \right) = 0, \tag{2.3}$$

where $\hat{n}_q$ is the unit normal vector of the plane, which can be estimated from

$$\vec{n}_q = (\vec{x}_q^C - \vec{x}_q^B) \times (\vec{x}_q^A - \vec{x}_q^B). \tag{2.4}$$

We use (2.2) and (2.3) to solve for q and thereby $\vec{r}_q^u$. Now, $\vec{r}_q^u$ lies within the triangle if

$$\begin{aligned} \vec{n}_q \cdot \left((\vec{x}_q^B - \vec{x}_q^A) \times (\vec{r}_q^u - \vec{x}_q^A) \right) &> 0, \\ \vec{n}_q \cdot \left((\vec{x}_q^C - \vec{x}_q^B) \times (\vec{r}_q^u - \vec{x}_q^B) \right) &> 0, \\ \vec{n}_q \cdot \left((\vec{x}_q^A - \vec{x}_q^C) \times (\vec{r}_q^u - \vec{x}_q^C) \right) &> 0. \end{aligned} \tag{2.5}$$

Based on the above mathematical formulations, there can be three possibilities: A ray may not intersect any facet on the human body if the intersection point does not lie within any triangle; or it may intersect just one facet of the body; or it may intersect more than one facets as shown in Fig. 2.2. In the first case, there will be no scattered response from the body due to ray u. In the last case, we assume that only the facet nearest to Ω_I (lowest value of parameter q in (2.2)) scatters the signal while the remaining facets are in shadow and do not contribute to the scattered field.

2.3 Reflected rays

The scattered electric field from the qth facet at any point $\vec{r}^s$ is described by

$$\vec{E}_q^r(\vec{r}^s) = \left(\hat{h} E_q^{r,h} + \hat{z} E_q^{r,v} \right) e^{-jk\hat{\phi}_q^r \cdot \vec{r}^s}, \tag{2.6}$$

where $\hat{h} E_q^{r,h}$ and $\hat{z} E_q^{r,v}$ are the horizontal and vertical polarization components respectively. The direction of the reflected ray, $\hat{\phi}_q^r$, is estimated from Snell's law by

$$\hat{\phi}_q^r = \hat{\phi}^i - 2(\hat{\phi}^i \cdot \hat{n}_q)\hat{n}_q. \tag{2.7}$$

The human body is a complex dielectric medium of skin, tissues and bone. However, at high frequencies (24 GHz and 77 GHz), there is little penetration through the skin and therefore, we model the human body as a single layer dielectric with relative permeability $\epsilon_r'(f_c) = \epsilon_r(f_c) - \frac{\sigma_c(f_c)}{j2\pi f_c \epsilon_0}$. The dielectric constant and conductivity are $\epsilon_r = 6.63$ and $\sigma_c = 38.1$ S/m at 77 GHz [37] and $\epsilon_r = 50$ and $\sigma_c = 1$ S/m at 24 GHz [31, 33]. The incident electric field is transformed to the local vertical, $\vec{E}^{i,v'}$, and horizontal polarization, $\vec{E}^{i,h'}$ components corresponding to the plane of the triangle. If ψ is the angle between $\hat{\phi}^i$ and $\hat{n}_q$, then the planar horizontal and vertical reflection

coefficients, $\Gamma_q^{h'}$ and $\Gamma_q^{v'}$ are given by

$$
\begin{aligned}
\Gamma_q^{h'} &= \frac{\cos\psi - \sqrt{\epsilon_r'}\sqrt{1 - \frac{\sin^2\psi}{\epsilon_r'}}}{\cos\psi + \sqrt{\epsilon_r'}\sqrt{1 - \frac{\sin^2\psi}{\epsilon_r'}}} \\
\Gamma_q^{v'} &= \frac{-\cos\psi + \sqrt{\frac{1}{\epsilon_r'}}\sqrt{1 - \frac{\sin^2\psi}{\epsilon_r'}}}{\cos\psi + \sqrt{\frac{1}{\epsilon_r'}}\sqrt{1 - \frac{\sin^2\psi}{\epsilon_r'}}}.
\end{aligned}
\tag{2.8}
$$

The strength of the reflected field $\vec{E}_q^r$ components are given by

$$
E_q^{r,h} = \left(\Gamma_q^{h'} E^{i,h'}\hat{h}' + \Gamma_q^{v'} E^{i,v'}\hat{v}'\right) e^{-jk\zeta} \cdot \hat{h} \tag{2.9}
$$

$$
E_q^{r,v} = \left(\Gamma_q^{h'} E^{i,h'}\hat{h}' + \Gamma_q^{v'} E^{i,v'}\hat{v}'\right) e^{-jk\zeta} \cdot \hat{z}, \tag{2.10}
$$

where ζ is the path difference travelled by the wave $|\vec{r}_q^u - \vec{r}^u|$. The reflected rays or *secondary rays* may return to the radar receiver or may bounce off other body parts giving rise to tertiary rays and so on. The reflected rays (secondary, tertiary or higher order) that return to the radar receiver are modelled as falling on an exit aperture Ω_E parallel to Ω_I. For each bounce off a body part, the steps from (2.2) to (2.7) are repeated. The amplitude of the field falls for each successive bounce while the phase of the field is estimated from the path travelled by the rays.

2.4 Back-scattered rays and RCS calculation

The scattered field at the exit aperture plane, $\vec{E}^s(\vec{r}^e)$, is distributed in a non-uniform manner in the aperture plane where $\vec{r}^e$ indicates the intersection of the scattered ray with Ω_E. We perform a two-dimensional interpolation to obtain the scattered field across the uniform grid points on Ω_E. Then, the scattered field in a direction $\hat{\phi}^s$ is given by integrating the scattered electric field across the whole aperture Ω_E. The resulting fields have both the horizontal and vertical polarization components. Hence, we can estimate four types of RCS. They are the co-polarized horizontal (σ^{hh}) and vertical RCS (σ^{vv}) as well as the cross-polarized RCS (σ^{hv} and

$\sigma^{\mathrm{vh}})$.

$$\sigma^{\mathrm{hh}} = 4\pi \left| \frac{jk}{2\pi} \iint_{\Omega_E} \frac{E^{r,h}}{E^{i,h}} e^{jk\hat{\phi}^s \cdot \vec{r}^e} ds \right|^2 \tag{2.11}$$

$$\sigma^{\mathrm{vh}} = 4\pi \left| \frac{jk}{2\pi} \iint_{\Omega_E} \frac{E^{r,v}}{E^{i,h}} e^{jk\hat{\phi}^s \cdot \vec{r}^e} ds \right|^2 \tag{2.12}$$

$$\sigma^{\mathrm{hv}} = 4\pi \left| \frac{jk}{2\pi} \iint_{\Omega_E} \frac{E^{r,h}}{E^{i,v}} e^{jk\hat{\phi}^s \cdot \vec{r}^e} ds \right|^2 \tag{2.13}$$

$$\sigma^{\mathrm{vv}} = 4\pi \left| \frac{jk}{2\pi} \iint_{\Omega_E} \frac{E^{r,v}}{E^{i,v}} e^{jk\hat{\phi}^s \cdot \vec{r}^e} ds \right|^2. \tag{2.14}$$

Based on the incident and scattered angles ϕ^i and ϕ^s, we can compute the bistatic RCS for both types of polarizations. When $\phi^s = \phi^i$, the RCS corresponds to the monostatic case.

Chapter 3

Proposed method: Estimation of scattering coefficients of point scatterer model using RCS from ray tracing

The ray tracing method described above provides accurate estimates of the RCS of the whole human body based on the posture described by each frame of the MoCap data. However, the technique still remains computationally expensive and cannot be used to generate radar data at high radar sampling frequencies. Hence, ray tracing results cannot be directly used for generating radar signatures - such as range-time, Doppler-time and range-Doppler plots - of extended targets such as humans. In this chapter, we propose a method to obtain the radar signatures by hybridizing the ray tracing results and the scattering center model using the MoCap data.

3.1 Radar signal model

We begin by assuming that a monostatic radar is located at the origin. We model the radar transmit waveform as a frequency modulated continuous waveform (FMCW) of center carrier frequency f_c, radar bandwidth (BW) and chirp factor ($\gamma = BW/T_{\text{upchirp}}$) as shown in Fig. 3.1. The transmit signal, $x_p(\tau)$, over a single p^{th} pulse repetition interval (PRI), T_{PRI}, is given by

$$x_p(\tau) = \text{rect}\left(\frac{\tau}{T_{\text{PRI}}}\right) e^{j(2\pi f_c \tau + \pi \gamma \tau^2)}, \tag{3.1}$$

where

$$\text{rect}\left(\frac{\tau}{T_{\text{PRI}}}\right) = \begin{cases} 1, & 0 \leq \tau \leq T_{\text{upchirp}} \\ 0, & T_{\text{upchirp}} < \tau < T_{\text{PRI}}. \end{cases} \tag{3.2}$$

The interval between the up chirp duration T_{upchirp} and T_{PRI} may be regarded as dead time. We assume that the transmitted waveform spans T_{long} duration consisting of
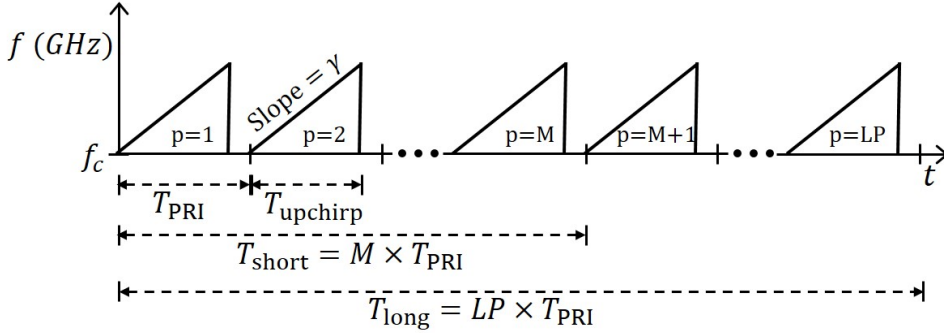
Figure 3.1: Radar signal model of linear frequency modulated continuous waveform of T_{upchirp} duration with chirp rate γ and T_{PRI} pulse repetition interval (PRI). Each T_{upchirp} consists of N samples of $f_s = \frac{1}{T_s}$ sampling frequency. T_{long} is the duration of L coherent processing intervals (CPI) each consisting of P PRIs. T_{short} is the time interval between M PRIs within T_{long}.

L coherent processing intervals (CPI) each of P PRIs. The radar signal falls upon a dynamic target of B point scatterers with scattering coefficients or reflectivities, $\{a_b, \ b = 1 : B\}$, which are assumed to be constant over the radar bandwidth and over the duration of T_{long}. If the time-varying radial distance of each of bth point scatterer with respect to the radar is $r_b(t)$, then the approximate baseband received signal can be written as

$$y(\tau, t) \approx \sum_{b=1}^{B} a_b \, \text{rect}\left(\frac{\tau - \frac{2r_b(t)}{c}}{T_{\text{PRI}}}\right)$$
$$\exp\left(-j2\pi f_c \frac{2r_b(t)}{c}\right) \exp\left(j\pi\gamma \left(\tau - \frac{2r_b(t)}{c}\right)^2\right), \tag{3.3}$$

where c is the velocity of light. The model in (3.3) is called the *primitive model* or *scattering center* model. The scattering center model is computationally simple

to execute the radar signatures, provided the positions and scattering coefficients of the scattering centers are available. Generally, the scattering centers are assumed to correspond to trackers placed on the live subject whose positions are gathered using MoCap technology. The position vector data is spline interpolated from the video frame rate ($\frac{1}{T_f}$) to the pulse repetition frequency ($\frac{1}{T_{\text{PRI}}}$) of the radar. In prior works, the scattering coefficients, a_b, have been estimated from the size, shape and orientation of primitives of body parts corresponding to the scattering centers [19, 26]. For example, a marker placed on the human arm corresponds to an ellipsoid of dimensions comparable to the human arm. The approximate nature of the scattering center coefficient results in very poor accuracy in the magnitude of the radar signatures. We propose to use the ray tracing results to obtain more accurate estimates of the scattering coefficients.

Based on the radar sampling frequency and pulse repetition frequency, the nth fast time sample of the discrete received signal for the pth PRI is

$$
\begin{aligned}
\boldsymbol{Y}[nT_s, pT_{\text{PRI}}] = \boldsymbol{Y}[n, p] = \sum_{b=1}^{B} a_b \, \text{rect}\left(\frac{n - \frac{2r_b[p]}{cT_s}}{N}\right) \\
\exp\left(-j2\pi f_c \frac{2r_b[p]}{c}\right) \exp\left(j\pi\gamma\left(nT_s - \frac{2r_b[p]}{c}\right)^2\right),
\end{aligned}
\tag{3.4}
$$

where $\{p = 1 : LP\}$ and $\{n = 1 : N\}$.

3.2 Linear regression model

The ray tracing techniques, described in the previous section, provided the RCS estimates ($\sigma^{\text{vv}}[fT_f], \sigma^{\text{hh}}[fT_f]$) at f_c for the whole human body at the video frame rate ($\frac{1}{T_f}$) of the MoCap data. Since vertical co-polarization is the most commonly used framework in automotive scenarios, we interpolate $\sigma^{\text{vv}}[f]$ to radar pulse repetition frequency ($\frac{1}{T_{\text{PRI}}}$) to get $\sigma^{\text{vv}}[p]$. The scattering coefficients can be assumed to be uniform across the radar bandwidth at automotive radar frequencies. Therefore, $\sqrt{\sigma^{\text{vv}}[p]}$ may be regarded as the first fast time sample of the scattered signal in (3.4),

at every p^{th} PRI with $\gamma = 0$ (ray tracing is applied at single frequency).

$$\sqrt{\sigma^{\text{vv}}[p]} = \boldsymbol{Y}[n=1,p] = \sum_{b=1}^{B} a_b \exp\left(-j2\pi f_c \frac{2r_b[p]}{c}\right). \tag{3.5}$$

Now if we assume that for slow moving humans, the reflectivities of the point scatterers (a_b) fluctuate very slowly across L CPIs (T_{long}) but the positions of the point scatterers ($\vec{r}_b$) change significantly across M PRIs ($T_{\text{short}} = M \times T_{\text{PRI}}$), we can frame a linear regression model $\boldsymbol{\Phi A} = \boldsymbol{\Psi}$ using

$$\boldsymbol{\Phi} = \begin{bmatrix} e^{-j2\pi f_c \frac{2r_1[1]}{c}} & e^{-j2\pi f_c \frac{2r_2[1]}{c}} & \dots & e^{-j2\pi f_c \frac{2r_B[1]}{c}} \\ e^{-j2\pi f_c \frac{2r_1[M]}{c}} & e^{-j2\pi f_c \frac{2r_2[M]}{c}} & \dots & e^{-j2\pi f_c \frac{2r_B[M]}{c}} \\ \vdots & \vdots & \ddots & \vdots \\ e^{-j2\pi f_c \frac{2r_1[LP]}{c}} & e^{-j2\pi f_c \frac{2r_2[LP]}{c}} & \dots & e^{-j2\pi f_c \frac{2r_B[LP]}{c}} \end{bmatrix} \tag{3.6}$$

and

$$\boldsymbol{A} = \begin{bmatrix} a_1 \\ a_2 \\ \vdots \\ a_B \end{bmatrix}, \boldsymbol{\Psi} = \begin{bmatrix} \sqrt{\sigma^{\text{vv}}[1]} \\ \sqrt{\sigma^{\text{vv}}[M]} \\ \vdots \\ \sqrt{\sigma^{\text{vv}}[LP]} \end{bmatrix}. \tag{3.7}$$

The integer number of rows of $\boldsymbol{\Phi} \in \mathbb{C}^{K \times B}$ is obtained by rounding $\lfloor \frac{LP}{M} \rfloor$ to the nearest integer. We estimate the reflectivities of the B point scatterers by solving for $\boldsymbol{A}$ using ordinary least squares ($\min_{\boldsymbol{A}} ||\boldsymbol{\Psi} - \boldsymbol{\Phi A}||_2^2$) [38], as shown below

$$\boldsymbol{A} = \left(\boldsymbol{\Phi}^T \boldsymbol{\Phi}\right)^{-1} \boldsymbol{\Phi}^T \boldsymbol{\Psi}. \tag{3.8}$$

Once the scattering center coefficients are estimated, they can be used in (3.4) to obtain the radar received data $\boldsymbol{Y}[n,p]$. The choices of L (and thereby T_{long}) as well as M (and T_{short}) are critical while P is fixed by the radar specifications. Since humans are typically slow moving targets, low values of T_{short} will result in very small changes between $r_b[p]$ and $r_b[p+M]$. This could result in singularity errors

15

in the solution. On the other hand, large values of T_{short} will result in long T_{long} intervals which is undesirable since the scattering coefficients are unlikely to remain unchanged over long durations.

In the above method, we have discussed how to estimate a_b for a monostatic radar configuration of vertically polarized radar. However, the method can be easily modified to allow considerable flexibility in terms of radar carrier frequency, bandwidth, radar position, aspect angles and polarization.

- Depending on the polarization requirement of the simulation framework, we can generate radar data by selecting corresponding RCS values ($\sigma^{\text{vv}}, \sigma^{\text{hh}}, \sigma^{\text{vh}}$ and σ^{hv}) computed from ray tracing for (3.5).

- Similarly, we can change from monostatic to bistatic radar configuration in (3.3). We can obtain the bistatic radar signatures by choosing the bistatic RCS values computed from ray tracing.

3.3 Generation of radar signatures

The two-dimensional radar data $\boldsymbol{Y}[n, p]$ along the fast and slow time axes are processed through Fourier transform to obtain three types of radar signatures for every T_{long} duration. The three signatures are: range-time ($\tilde{\chi}^{\text{RT}}$), Doppler-time ($\tilde{\chi}^{\text{DT}}$) and time-varying range-Doppler ambiguity plots ($\tilde{\chi}^{\text{RD}}$). As mentioned earlier, each T_{long} interval of the radar data consists of L CPIs each of P PRIs.

3.3.1 Range-time profile

The high resolution range-time profile is generated by implementing the one-dimensional Fourier transform on $\boldsymbol{Y}[n, p]$ along the fast time axis for each pth PRI as shown in

$$\tilde{\chi}_p^{\text{RT}}[g \Delta r] = \tilde{\chi}_p^{\text{RT}}[g] = \sum_{n=1}^{N} \boldsymbol{Y}[n, p] \boldsymbol{H}_{1D}[n] e^{-j \frac{2\pi g n}{N}},$$

$$g = \frac{-N}{2} : \frac{N}{2} - 1 \tag{3.9}$$

16

where, $\Delta r = \frac{c}{2BW}$ is range resolution and $\boldsymbol{H}_{1D}[\cdot] \in \mathbb{R}^{N \times 1}$ is a one-dimensional window function.

3.3.2   Doppler / velocity spectrogram

The Doppler spectrogram is generated by implementing the one-dimensional Fourier transform on $\boldsymbol{Y}[n = 1, p]$ along the slow time axis for each lth CPI as shown in

$$\tilde{\chi}_l^{\text{DT}}[d\Delta f_D] = \tilde{\chi}_l^{\text{DT}}[d] = \sum_{p=(l-1)P+1}^{lP} \boldsymbol{Y}[n = 1, p]\boldsymbol{H}_{1D}[p]e^{-j\frac{2\pi dp}{P}}, \tag{3.10}$$
$$d = \frac{-P}{2} : \frac{P}{2} - 1$$

where, $\Delta f_D = \frac{1}{PT_{\text{PRI}}}$ is Doppler resolution.

3.3.3   Range-Doppler ambiguity plots

Range-Doppler ambiguity plots are generated for each lth CPI through two-dimensional Fourier transform of $\boldsymbol{Y}[n, p]$ along the fast and slow time axes as shown below

$$\tilde{\chi}_l^{\text{RD}}[g, d] = \sum_{p=(l-1)P+1}^{lP} \sum_{n=1}^{N} \boldsymbol{Y}[n, p]\boldsymbol{H}_{2D}[n, p]e^{-j\frac{2\pi gn}{N}}e^{-j\frac{2\pi dp}{P}}, \tag{3.11}$$

where, $\boldsymbol{H}_{2D}[\cdot] \in \mathbb{R}^{N \times P}$ is a two-dimensional window function. The process is repeated across all the L CPIs to obtain the time-varying range-Doppler ambiguity plots.

The algorithm 1 summarizes the proposed simulation methodology to generate the radar signatures with accurate scattering center coefficients for every T_{long} period.

Algorithm 1 Simulation of radar signatures for every $T_{\text{long}} = LP\,T_{\text{PRI}}$

Input: MoCap data of B point scatterers on the human body at video frame rate $(\frac{1}{T_f})$: $\{\vec{r}_b[fT_f] = \vec{r}_b[f],\, b = 1:B\}$

1. Implement ray tracing on three-dimensional poly-mesh structure obtained from stick figure for every frame $\sigma^{\text{vv}}[f], f = 1:F$

2. Spline interpolate frames $\{f = 1:F\}$ of position vector of point scatterer data along with the RCS derived from ray tracing from video frame rate to radar pulse repetition frequency $(\frac{1}{T_{\text{PRI}}})$ to obtain $\{p = 1:LP\}$ values.

   (i) $\vec{r}_b[f] \longrightarrow \vec{r}_b[p]$

   (ii) $\sigma^{\text{vv}}[f] \longrightarrow \sigma^{\text{vv}}[p]$

3. Formulate $\mathbf{\Phi} \in \mathbb{C}^{K \times B}$ where $K = \lfloor \frac{LP}{M} \rfloor \approx B$ such that

$$
\mathbf{\Phi} = \begin{bmatrix}
e^{-j2\pi f_c \frac{2r_1[1]}{c}} & \cdots & e^{-j2\pi f_c \frac{2r_B[1]}{c}} \\
e^{-j2\pi f_c \frac{2r_1[M]}{c}} & \cdots & e^{-j2\pi f_c \frac{2r_B[M]}{c}} \\
\vdots & \ddots & \vdots \\
e^{-j2\pi f_c \frac{2r_1[LP]}{c}} & \cdots & e^{-j2\pi f_c \frac{2r_B[LP]}{c}}
\end{bmatrix}.
$$

   Also formulate

$$
\mathbf{A} = \begin{bmatrix} a_1 \\ a_2 \\ \vdots \\ a_B \end{bmatrix}, \mathbf{\Psi} = \begin{bmatrix} \sqrt{\sigma^{\text{vv}}[1]} \\ \sqrt{\sigma^{\text{vv}}[M]} \\ \vdots \\ \sqrt{\sigma^{\text{vv}}[LP]} \end{bmatrix}.
$$

4. Estimate the reflectivities of B point scatterers by $\mathbf{A} = \left(\mathbf{\Phi}^T\mathbf{\Phi}\right)^{-1}\mathbf{\Phi}^T\mathbf{\Psi}$ using ordinary least squares minimization of $||\mathbf{\Psi} - \mathbf{\Phi}\mathbf{A}||_2^2$.

5. **Output:** Model received radar signal using position and estimated reflectivities of point scatterers for every n^{th} fast time sample of pth PRI.

$$
\mathbf{Y}[n,p] = \sum_{b=1}^{B} a_b \, \text{rect}\left(\frac{n - \frac{2r_b[p]}{cT_s}}{N}\right) \exp\left(-j2\pi f_c \frac{2r_b[p]}{c}\right)
$$
$$
\exp\left(j\pi\gamma\left(nT_s - \frac{2r_b[p]}{c}\right)^2\right).
$$

6. Use $\mathbf{Y}[n,p]$ to obtain three types of radar signatures:

   • Implement 1D Fourier transform on $\mathbf{Y}[n,p]$ along fast time axis (n) for every p^{th} PRI to obtain radar range-time signature $(\tilde{\chi}^{\text{RT}})$.

   • Implement 1D Fourier transform on $\mathbf{Y}[n,p]$ along slow time axis (p) for every CPI (P PRIs) to obtain Doppler-time spectrogram $(\tilde{\chi}^{\text{DT}})$.

   18

   • Implement 2D Fourier transform on $\mathbf{Y}[n,p]$ to obtain range-Doppler ambiguity plot $(\tilde{\chi}^{\text{RD}})$.

Chapter 4

Experimental Results and Analysis

In this chapter we present the experimental results for validating the proposed methodology. We collect MoCap data of human motion and use it to simulate radar data. Simultaneously, we collect hardware based radar data for the same human subject from a measurement setup at 77 GHz. The experimental setup is discussed in the following section. We perform ray tracing on the three-dimensional poly-mesh structure obtained from the stick figure animation of every frame of the MoCap data to simulate the monostatic RCS of the pedestrian for vertical polarization. Then we use these values to generate scattering coefficients of the scattering center model of a human. Finally, we generate the simulated radar signatures which we compare with measurement results.

4.1 Experimental data collection

We consider a human subject moving along the trajectory shown in Fig. 4.1. We collect MoCap data of the human motion using Xsens MTw Awinda [39], an inertial measurement unit containing three-dimensional linear accelerometers and rate gyroscopes. 17 trackers (front and back side) are attached to defined locations on the subject's body to measure the motion of each body segment. Additionally, position information of 6 other body segments on the torso and feet are determined by interpolation by the MoCap software. Wireless communication between the sensors and the synchronization station takes place at 60 Hz frame rate. The MoCap data of the 23 markers are used for simulating the radar returns. For validation purposes, the radar returns from the subject is simultaneously captured using a 77 GHz linear frequency modulated INRAS RadarLog sensor [40, 41]. The simulation parameters for

19

the radar signal model discussed in chapter 3 are chosen to match the radar hardware configurations as listed in Table 4.1.
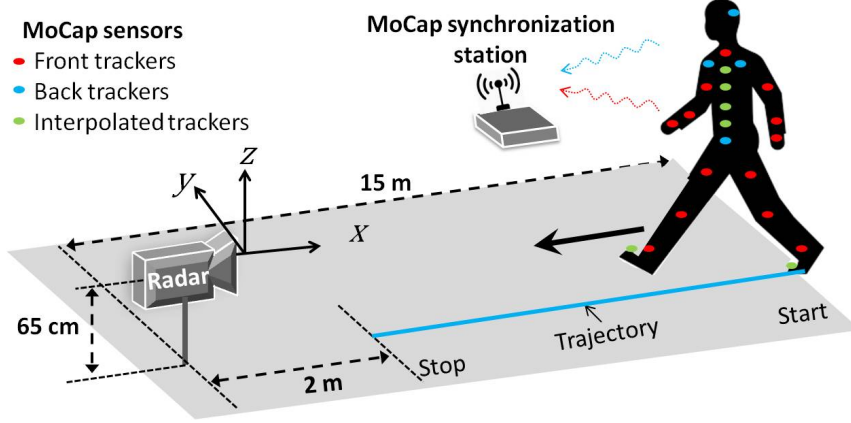
Figure 4.1: Subject wearing 17 trackers in front (red) and back (blue) view; 6 interpolated trackers (green), for collecting MoCap data, walks radially towards the radar sensor (INSAR RadarLog) from 15 m distance and stops 2 m before the radar along the trajectory (indicated by blue line). The radar sensor is positioned at [0, 0, 0.65] m. The wireless communication between the MoCap sensors and the synchronization station takes place at 60 Hz frame rate.

Radar parameters	
Carrier frequency (f_c)	77 GHz
Bandwidth (BW)	2 GHz
Sampling frequency (f_s)	10 MHz
Up Chirp duration (T_{upchirp})	51.2 μs
Pulse repetition interval (T_{PRI})	61.2 μs
No. of chirps per CPI (P)	1024
Range resolution (Δr)	7.5 cm
Doppler resolution (Δf_D)	15.9 Hz
Radar sensor position	[0, 0, 0.65] m

Table 4.1: Radar parameters used for simulation are chosen to match the INRAS RadarLog sensor.

4.2   Results from electromagnetic ray tracing

The animated stick figure model obtained from MoCap is embodied using an in-built library of a nude male in Poser Pro software from Smith Micro Inc. [29].

Each frame of the human body is subsequently rendered into a three-dimensional poly-mesh structure composed of 3052 triangular facets. The data for each frame consist of three-dimensional position coordinates of the triangle's vertices which are exported to MATLAB for further processing. We present the results for illumination at three aspect angles: $\phi^i = 0°$, $45°$ and $90°$. Fig. 4.2 shows a single frame / pose of a walking human illuminated by a vertically polarized incident electric field at 77 GHz. The strength of the scattered field from the different human body parts is determined by the aspect of the target. The thighs and torso of the body scatter stronger signals than the other body parts (like head or hands). In all the cases, it is evident that some of the body parts are shadowed from the incident field. The strongest illumination is observed at frontal incidence $\phi^i = 0°$.
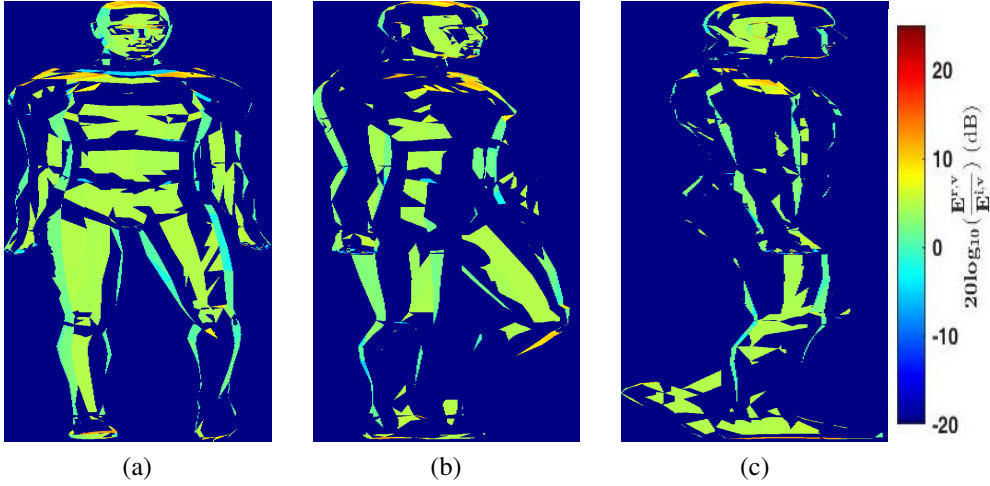
Figure 4.2: A single frame/pose of dynamic human motion illuminated by a vertically polarized incident electric field at 77 GHz for three aspect angles (a) front incidence ($\phi^i = 0°$) (b) oblique incidence ($\phi^i = 45°$) and (c) $90°$ incidence ($\phi^i = 90°$).

Based on the scattered signal from all the body parts, we estimate the total monostatic RCS of the human at every frame of the MoCap data. We present the results for a complete walking stride - the full swing motion of a hand/leg - of 69 frames from $2.8\,\mathrm{s}$ to $3.9\,\mathrm{s}$ for the three different incident aspect angles of $0°, 45°$ and $90°$ at 77 GHz in Fig. 4.3a - 4.3c and at 24 GHz, the other popular band of carrier frequencies for automotive radar [42], in Fig. 4.3d - 4.3f. The figure shows that the co-polarization (σ^{vv} and σ^{hh}) components range from -10 dBsm to +5 dBsm. The cross-polarization com-
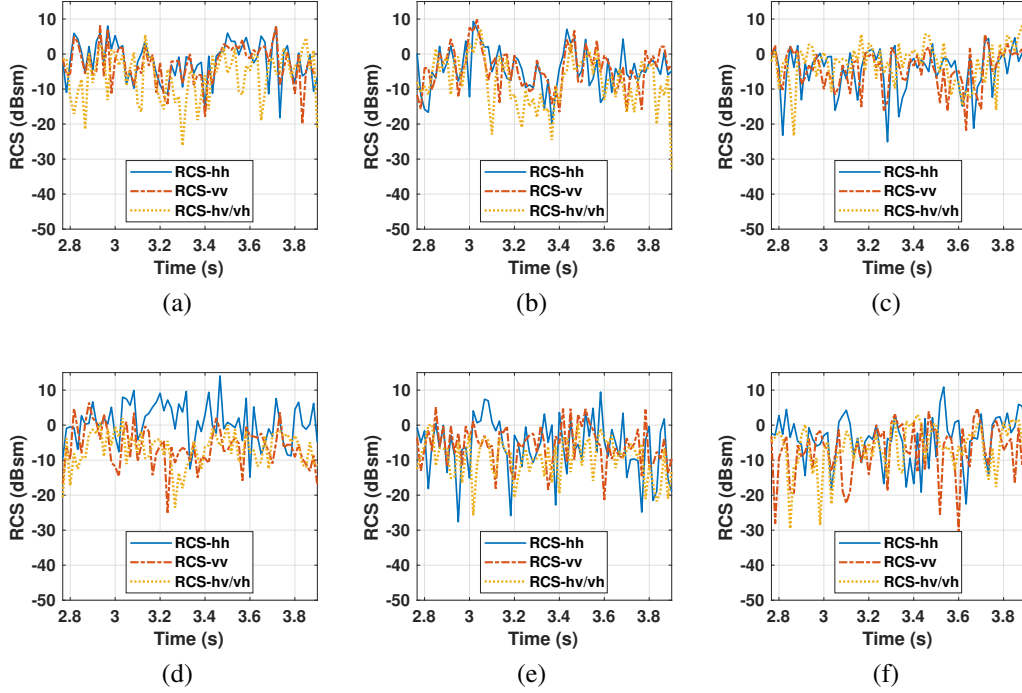
Figure 4.3: Simulated monostatic ($\phi^i = \phi^s$) RCS across multiple frames corresponding to one walking stride obtained from ray tracing for three aspect angles (a) front incidence ($\phi^i = 0°$) (b) oblique incidence ($\phi^i = 45°$) and (c) 90° incidence ($\phi^i = 90°$) at 77 GHz and (d) - (f) at 24 GHz.

ponents are generally weaker by approximately 10 dB. These RCS values are within the range of those reported from measurement studies of pedestrians at X-band frequencies [33, 43]. Fig. 4.3d - 4.3f shows that the RCS values are slightly higher for the horizontal co-polarization scenario when compared to the vertical polarization especially for the case of frontal incidence (0°) at 24 GHz. On average, the frontal incidence also gives rise to the highest RCS values for the monostatic configuration.

In some $V2X$ applications, it may be useful to have bistatic RCS of pedestrians. Fig. 4.4, presents the variation of RCS with ϕ^s for bistatic angle $= \phi^s - \phi^i$; for a single frame/pose for different polarizations and for three different incident angles. The bistatic RCS corresponds to the monostatic RCS when $\phi^s = \phi^i$. Interesting, the bistatic RCS is higher than the monostatic RCS at some aspect angles for some postures of the human.
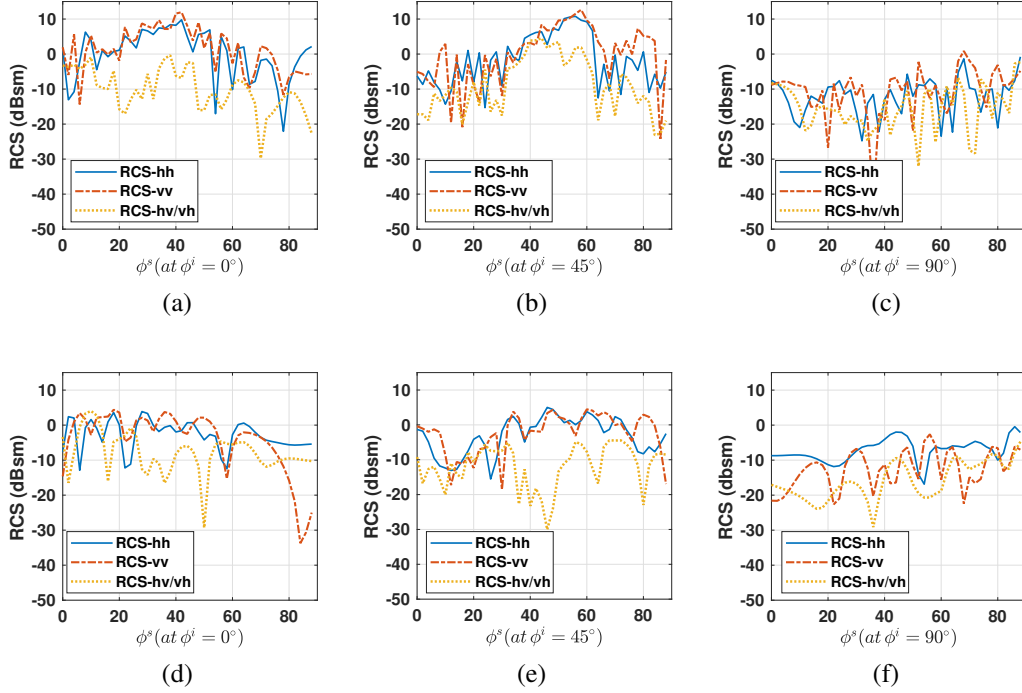
Figure 4.4: Simulated bistatic RCS versus ϕ^s such that bistatic aspect angle $= \phi^s - \phi^i$; for single frame/pose for three aspect angles (a) front incidence ($\phi^i = 0°$) (b) oblique incidence ($\phi^i = 45°$) and (c) $90°$ incidence ($\phi^i = 90°$) at 77 GHz and (d) - (f) at 24 GHz.

4.3 Radar signatures generated from simulated and measured radar data

All the results presented in the previous section were generated with ray tracing alone. The next set of results are generated by hybridization of ray tracing and point scatterer modeling. We use the vertical co-polarized RCS (σ^{vv}) values at front incidence ($\phi^i = 0°$) to match the radar hardware configurations. The scattering coefficients are estimated by solving the linear regression framework in (3.5) where T_{long} (and L) and T_{short} (and M) have to be carefully chosen. Both L and M determine K, the number of rows in $\mathbf{\Phi}$ matrix, since K is rounded to the nearest integer $\lfloor \frac{LP}{M} \rfloor$ and P is fixed.

Fig. 4.5a shows the average l_2 norm error, $\frac{||\mathbf{\Psi} - \mathbf{\Phi A}||_2^2}{||\mathbf{\Psi}||_2^2}$ for different values of K. When K is very large due to small values of M, we get very high errors. This is because for slow moving targets, such as humans, there is very small variation in the

23

position of some of the scatterers (such as torso) in consecutive T_{short} intervals. This results in singularities in the problem formulation. We find that the optimum results occur when $K \approx B$, that is when the $\boldsymbol{\Phi}$ matrix is close to a square matrix. Different
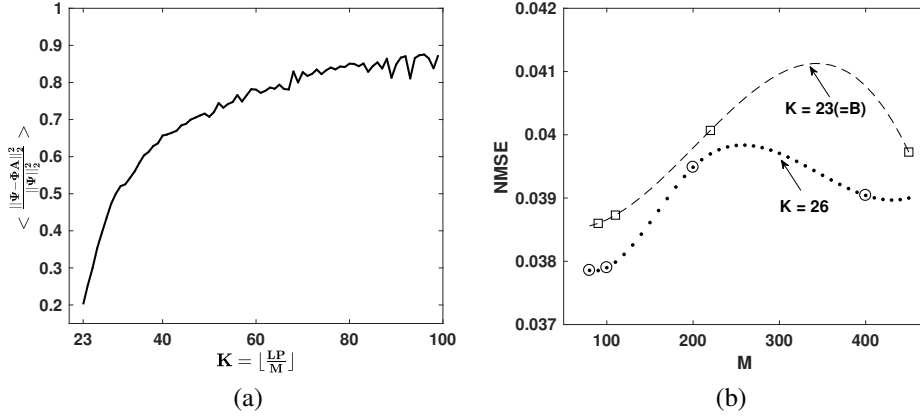
Figure 4.5: To make the choice of T_{long} (and L) and T_{short} (and M): (a) Estimation error $\frac{\|\boldsymbol{\Psi} - \boldsymbol{\Phi A}\|_2^2}{\|\boldsymbol{\Psi}\|_2^2}$ averaged over the number of estimations done for duration of target motion for different values of $K = \lfloor \frac{LP}{M} \rfloor$ is plotted. (b) Comparing the NMSE between simulated and measured range-time plots for $K = 23$ and $K = 26$ for different values of M.

combinations of L and M can result in similar values of K. However, when M is very large, this gives rise to a correspondingly large value of $L = \frac{MK}{P}$. But long T_{long} duration is undesirable since scattering coefficients are likely to fluctuate over long intervals due to variations in target aspect. We compared the NMSE of the measured and simulated range-time ambiguity plots for different M for a fixed $K = 23(= B)$ and $K = 26$ in Fig. 4.5b. The result shows that the NMSE is lesser for slightly over-determined matrix i.e., $K = 26(= B + 3)$. Based on the above studies, we determined $M = 80$ and $L = 2$ to be the optimum values for our simulation. Hence, the T_{long} and T_{short} used in the linear regression framework are 12.5 ms and 4.9 ms respectively.

We present three types of radar signatures - the high range-resolution profile, the Doppler-time spectrogram and the range-Doppler ambiguity plots and compare these signatures with those generated from measurement data collected from the radar hardware. The measurement data is suitably range compensated to obtain the time-

varying radar cross-section of the target. Since the measurement data is naturally corrupted by noise, an ordered statistics constant false alarm rate (OS-CFAR) algorithm based on [44] is implemented on the measurement data, which adaptively estimates the detection threshold for each cell based on neighboring cells. The CFAR algorithm is not required on the simulation data where noise is not considered. We present both qualitative and quantitative comparisons between the simulated and measured radar signatures.

First, we present the *high range-resolution profile* of the walking human in Fig. 4.6a and Fig. 4.6b. The figure on the top is generated from simulation data ($\tilde{\chi}^{RT}$) while the one in the bottom is from measurement data (χ^{RT}). Values below -40 dBsm threshold are not shown in both the figures. We observe that the human is first stationary for 1.5 s and then approaches the radar from a range of 15 m to 2 m from 1.5 s to 10.3 s. The swinging motion of the arms and legs give rise to micro-range features about the torso that spans approximately 1.5 m. The range ambiguity is 7 cm. Therefore, it is difficult in both figures to resolve the independent point scatterers from the different body parts along range. The simulated results closely resembles the measured results in terms of dynamic range. The torso appears to be the strongest component in both images when compared to the arms and legs. The range spread due to the spatial extent of the target is nearly identical in both the images (indicated by horizontal dashed lines). The vertical dashed lines in both the figures indicate the similarity in time span also. Thus visually, there is structural similarity in the images.

Next, we examine the *Doppler-spectrograms* from the simulated ($\tilde{\chi}^{DT}$) and measured data (χ^{DT}) in Fig. 4.6c and Fig. 4.6d. Since the human is approaching the radar, the Dopplers are mostly positive with some negative Dopplers due to the back swing of the arms and legs. The human is walking at a velocity of approximately 1.5 m/s. This results in a strong torso Doppler component in both images. We can observe much weaker micro-Dopplers from the arms and legs up to velocities of 5 m/s. The Doppler span for measurement results are slightly higher than the simulated results due to noise characteristics. The periodicity of the strides in the two figures shows excellent agreement. There is a strong DC component in the simulation figure
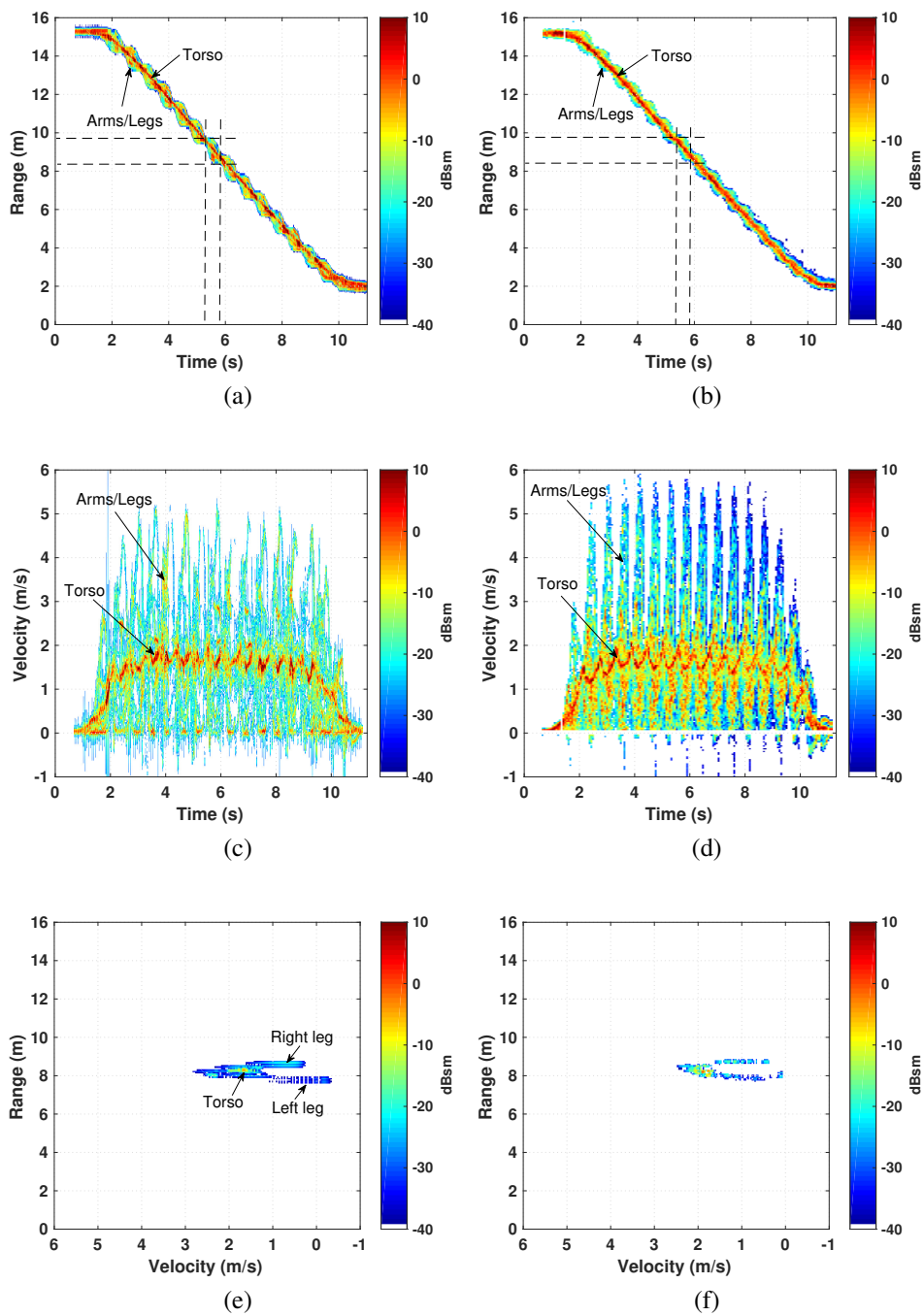
Figure 4.6: Simulated (a, c, e) and measured (b, d, f) radar signatures of a human walking towards a 77 GHz monostatic radar. Figures (a) and (b) correspond to range-time ambiguity plot; (c) and (d) correspond to Doppler-time ambiguity plots; and (e) and (f) correspond to range-Doppler ambiguity plot for one CPI (from 6.16 to 6.22 seconds).

that is not present in the measurement results due to a DC filter in the radar hardware to eliminate static clutter.

Finally, we present the *range-Doppler ambiguity plot* for a single CPI (from 6.16 to 6.22 seconds) in Fig. 4.6e and Fig. 4.6f. Here we observe that the range and Doppler ambiguities in both the simulated ($\tilde{\chi}^{\text{RD}}$) and measured data (χ^{RD}) are nearly identical. We are now able to resolve the arms, legs and torso in the ambiguity plots. The simulation result enables us to correctly identify the different body parts. Again the peak and dynamic range of the two plots are very similar.

4.3.1   Quantitative comparison

In the above discussion, we have qualitatively compared the simulated and measured results. Next, we perform a quantitative comparison between the two signatures in the form of two metrics - the normalized mean square error (NMSE) and the structural symmetry index (SSIM). The NMSE for the range time plot is computed by

$$NMSE = \frac{||\tilde{\chi}^{\text{RT}} - \chi^{\text{RT}}||_2^2}{||\chi^{\text{RT}}||_2^2}. \tag{4.1}$$

The SSIM is a metric used for comparing structural differences such as luminance and contrast between two images [45]. It is computed by

$$SSIM = \frac{(2E[\tilde{\chi}]E[\chi])(2\text{covar}[\tilde{\chi}, \chi])}{(E^2[\tilde{\chi}] + E^2[\chi])(\text{var}[\tilde{\chi}] + \text{var}[\chi])}, \tag{4.2}$$

where $E[\cdot]$, $\text{var}[\cdot]$ and $\text{covar}[\cdot]$ denote mean, variance and co-variance of the two images. When the images are identical, its value is 1.

Table 4.2 shows the NMSE and SSIM for the three radar signatures for the duration of the target motion. All three signatures show low values of NMSE, and SSIM values close to 1 which indicates the close similarity between the simulation and measurement data.

Fig. 4.7 shows the NMSE and the SSIM between the simulated and measured range-Doppler ambiguity plots over the duration of one walking stride (9 T_{long}) from

27

	Range-time	Doppler-spectrograms	Range-Doppler
SSIM	0.86	0.81	0.99
NMSE	0.04	0.10	0.03

Table 4.2: Quantitative comparison between simulated and measured range-time, Doppler-time and range-Doppler plots through NMSE and SSIM values for the duration of target motion

5.76 to 6.89 seconds.
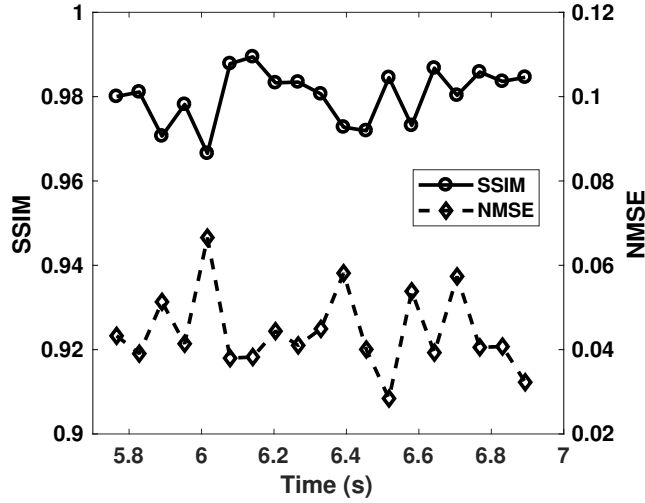
Figure 4.7: SSIM and NMSE values for range-Doppler plots for one complete walking stride from 5.76 to 6.89 seconds.

The results in the figure show the range of SSIM between 0.96 to 0.99 which is close to ideal. The NMSE is likewise close to zero.

The computational complexity of the proposed approach required ray tracing to be carried out at video frame rate, matrix inversion operations for determining scattering coefficients and linear operations for point scatterer modeling at radar sampling frequencies. The matrix inversion operation is computationally not very hard due to the small size of the matrix ($[(K \approx B) \times B]$). Among these three steps, the ray tracing operation is the most computationally expensive. In Fig. 4.8, we indicate the computational time for generating the results for different processing configurations.

28

A realistic model of the human requires the body to be rendered by a large number of small sized triangular facets for ray tracing. The illumination rays must, likewise, be densely placed (at least $\frac{\lambda}{10}$ apart) to get an accurate RCS estimate. The computational complexity is determined by the intersection tests between all the illumination rays and the facets on the body. This results in considerable complexity (800 minutes to compute RCS at 77 GHz in Fig. 4.8).
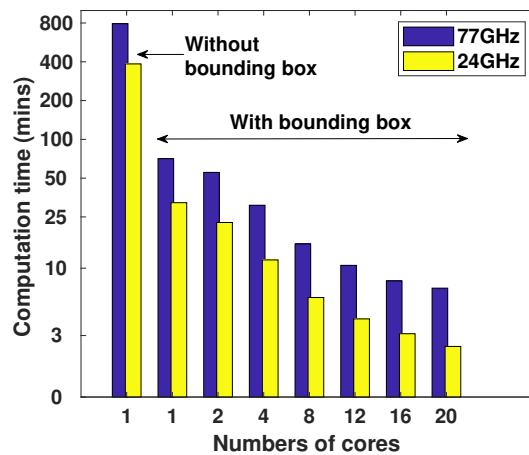
Figure 4.8: Reduction in computation time of RCS using electromagnetic ray tracing, with introduction of bounding box technique and increasing the number of cores for parallel processing at 77 GHz and 24 GHz

Several works in graphics have addressed the challenges of reducing the computational complexity associated with ray tracing [46, 47]. We have implemented the bounding box test in our work where the poly-mesh human is divided into several distinct parts each enclosed by a spatial bounding box. Instead of testing every ray with every triangle, we test every ray with every bounding box. Only if the ray intersects the bounding box, do we test the intersection of the ray with every facet within the bounding box. By using bounding box technique on a single core processor, we observed about 14 times reduction in computation time from 800 to 60 minutes in Fig. 4.8.

Since the ray-triangle intersection tests can be carried out in parallel, the computation time can be further reduced by implementing the algorithm across multiple parallel processors. The algorithm was implemented using the parallel computing tool box of Matlab.

By using the parallel processing with the bounding box technique, the computation time was further reduced to 8 minutes for a 20 core system.

Chapter 5

Conclusion

The shooting and bouncing ray technique based on ray tracing and geometric optics has been used extensively to accurately model the RCS of targets at high carrier frequencies. However, the technique is computationally extensive and hence not suitable for modeling the time-varying RCS of dynamic human motions, at radar sampling frequencies, since humans are spatially large three-dimensional dielectric bodies with considerable variation in posture and pose. A computationally simpler alternative for modeling radar signatures of human motion is based on the scattering center model. However, the reflectivities of the scattering centers, in prior works, have been loosely approximated by RCS values of primitives resembling body shapes resulting in inaccurate estimates of RCS magnitudes.

In our work, we hypothesize that the scattering coefficients fluctuate very slowly over multiple CPIs while the positions of the scatterers change rapidly across multiple PRIs. Therefore, we estimate the scattering center coefficients by combining the point scatterer model with the ray tracing RCS estimates in a linear regression framework. The positions of the scattering centers are obtained from an animation model of a pedestrian gathered from MoCap data. We use the reflectivity estimates to obtain realistic radar scattered signal that are processed to obtain commonly used radar signatures such as range-time, Doppler-time and range-Doppler ambiguity plots. Simultaneous to the MoCap data collection, we gathered measurement data using an automotive radar at 77 GHz from which the radar signatures were generated. The simulated signatures showed a low normalized mean square error (below 10%) and high structural similarity (above 80%) with respect to the measured signatures indicating the efficacy of the proposed method. We also demonstrated the versatility

of our simulation method for modeling radar signatures at different polarizations, aspect angles and carrier frequencies.

Bibliography

[1] W. H. Organization *et al.*, "More than 270 000 pedestrians killed on roads each year. 2013," 2017.

[2] D. C. Andrade, F. Bueno, F. R. Franco, R. A. Silva, J. H. Z. Neme, E. Margraf, W. T. Omoto, F. A. Farinelli, A. M. Tusset, S. Okida *et al.*, "A novel strategy for road lane detection and tracking based on a vehicle's forward monocular camera," *IEEE Transactions on Intelligent Transportation Systems*, no. 99, pp. 1–11, 2018.

[3] S. Silberstein, D. Levi, V. Kogan, and R. Gazit, "Vision-based pedestrian detection for rear-view cameras," in *Intelligent Vehicles Symposium Proceedings, 2014 IEEE*.   IEEE, 2014, pp. 853–860.

[4] E. Belyaev, P. Molchanov, A. Vinel, and Y. Koucheryavy, "The use of automotive radars in video-based overtaking assistance applications," *IEEE Transactions on Intelligent Transportation Systems*, vol. 14, no. 3, pp. 1035–1042, 2013.

[5] F. Engels, P. Heidenreich, A. M. Zoubir, F. K. Jondral, and M. Wintermantel, "Advances in automotive radar: A framework on computationally efficient high-resolution frequency estimation," *IEEE Signal Processing Magazine*, vol. 34, no. 2, pp. 36–46, 2017.

[6] A. Ghaleb, L. Vignaud, and J. Nicolas, "Micro-doppler analysis of wheels and pedestrians in isar imaging," *IET Signal Processing*, vol. 2, no. 3, pp. 301–311, 2008.

[7] Y. Kim and H. Ling, "Human activity classification based on micro-doppler signatures using a support vector machine," *IEEE Transactions on Geoscience and Remote Sensing*, vol. 47, no. 5, pp. 1328–1337, 2009.

[8] Y. Kim, S. Ha, and J. Kwon, "Human detection using doppler radar based on physical characteristics of targets," *IEEE Geoscience and Remote Sensing Letters*, vol. 12, no. 2, pp. 289–293, 2015.

[9] V. C. Chen and H. Ling, *Time-frequency transforms for radar imaging and signal analysis*. Artech House, 2002.

[10] B. G. Mobasseri and M. G. Amin, "A time-frequency classifier for human gait recognition," in *Optics and Photonics in Global Homeland Security V and Biometric Technology for Human Identification VI*, vol. 7306. International Society for Optics and Photonics, 2009, p. 730628.

[11] J. L. Geisheimer, E. F. Greneker, and W. S. Marshall, "High-resolution doppler model of the human gait," in *Radar Sensor Technology and Data Visualization*, vol. 4744. International Society for Optics and Photonics, 2002, pp. 8–19.

[12] P. Van Dorp and F. C. Groen, "Human motion estimation with multiple frequency modulated continuous wave radars," *IET radar, sonar & navigation*, vol. 4, no. 3, pp. 348–361, 2010.

[13] S. Ram and H. Ling, "Analysis of microdopplers from human gait using reassigned joint time-frequency transform," *Electronics Letters*, vol. 43, no. 23, 2007.

[14] H. Rohling, S. Heuel, and H. Ritter, "Pedestrian detection procedure integrated into an 24 ghz automotive radar," in *Radar Conference, 2010 IEEE*. IEEE, 2010, pp. 1229–1232.

[15] M. Stolz, E. Schubert, F. Meinl, M. Kunert, and W. Menzel, "Multi-target reflection point model of cyclists for automotive radar," in *Radar Conference (EURAD), 2017 European*. IEEE, 2017, pp. 94–97.

[16] A. Angelov, A. Robertson, R. Murray-Smith, and F. Fioranelli, "Practical classification of different moving targets using automotive radar and deep neural networks," *IET Radar, Sonar & Navigation*, 2018.

[17] S. Lee, Y.-J. Yoon, J.-E. Lee, and S.-C. Kim, "Human–vehicle classification using feature-based svm in 77-ghz automotive fmcw radar," *IET Radar, Sonar & Navigation*, vol. 11, no. 10, pp. 1589–1596, 2017.

[18] R. Prophet, M. Hoffmann, A. Ossowska, W. Malik, C. Sturm, and M. Vossiek, "Pedestrian classification for 79 ghz automotive radar systems," in *2018 IEEE Intelligent Vehicles Symposium (IV)*. IEEE, 2018, pp. 1265–1270.

[19] K. V. Mishra, S. S. Ram, S. Vishwakarma, and G. Duggal, "Doppler-resilient 802.11 ad-based ultra-short range automotive radar," *arXiv preprint arXiv:1902.01306*, 2019.

[20] S. S. Ram, C. Christianson, Y. Kim, and H. Ling, "Simulation and analysis of human micro-dopplers in through-wall environments," *IEEE Transactions on Geoscience and remote sensing*, vol. 48, no. 4, pp. 2015–2023, 2010.

[21] D. P. Fairchild and R. M. Narayanan, "Classification of human motions using empirical mode decomposition of human micro-doppler signatures," *IET Radar, Sonar & Navigation*, vol. 8, no. 5, pp. 425–434, 2014.

[22] L. Ren, N. Tran, F. Foroughian, K. Naishadham, J. E. Piou, O. Kilic, and A. E. Fathy, "Short-time state-space method for micro-doppler identification of walking subject using uwb impulse doppler radar," *IEEE Transactions on Microwave Theory and Techniques*, 2018.

[23] J. Park, J. T. Johnson, N. Majurec, M. Frankford, K. Stewart, G. E. Smith, and L. Westbrook, "Simulation and analysis of polarimetric radar signatures of human gaits," *IEEE Transactions on Aerospace and Electronic Systems*, vol. 50, no. 3, pp. 2164–2175, 2014.

[24] G. E. Smith, K. Woodbridge, and C. J. Baker, "Multistatic micro-doppler signature of personnel," in *Radar Conference, 2008. RADAR'08. IEEE*. IEEE, 2008, pp. 1–6.

[25] Y.-Y. Tsai, W.-C. Lin, K. B. Cheng, J. Lee, and T.-Y. Lee, "Real-time physics-based 3d biped character animation using an inverted pendulum model," *IEEE*

transactions on visualization and computer graphics, vol. 16, no. 2, pp. 325–337, 2010.

[26] R. Boulic, N. M. Thalmann, and D. Thalmann, "A global human walking model with real-time kinematic personification," *The visual computer*, vol. 6, no. 6, pp. 344–358, 1990.

[27] S. S. Ram and H. Ling, "Microdoppler signature simulation of computer animated human and animal motions," in *Antennas and Propagation Society International Symposium, 2008. AP-S 2008. IEEE.* IEEE, 2008, pp. 1–4.

[28] B. Erol and S. Z. Gurbuz, "A kinect-based human micro-doppler simulator," *IEEE Aerospace and Electronic Systems Magazine*, vol. 30, no. 5, pp. 6–17, 2015.

[29] S. M. Software, "Poser," http://my.smithmicro.com/poser-3d-animation-software.html.

[30] S. Chattopadhyay, S. M. Bhandarkar, and K. Li, "Human motion capture data compression by model-based indexing: A power aware approach," *IEEE transactions on visualization and computer graphics*, vol. 13, no. 1, pp. 5–14, 2007.

[31] T. Dogaru, L. Nguyen, and C. Le, "Computer models of the human body signature for sensing through the wall radar applications," Army Research Lab Adelphi, Tech. Rep., 2007.

[32] T. Dogaru and C. Le, "Validation of xpatch computer models for human body radar signature," Army Research Lab Adelphi, Tech. Rep., 2008.

[33] C. Le and T. Dogaru, "Numerical modeling of the airborne radar signature of dismount personnel in the uhf-, l-, ku-, and ka-bands," Army Research Lab Adelphi, Tech. Rep., 2007.

[34] P. van Dorp and F. Groen, "Human walking estimation with radar," *IEE Proceedings-Radar, Sonar and Navigation*, vol. 150, no. 5, pp. 356–365, 2003.

[35] A. F. Garcia-Fernandez, O. A. Yeste-Ojeda, and J. Grajal, "Facet model of moving targets for isar imaging and radar back-scattering simulation," *IEEE Transactions on Aerospace and Electronic Systems*, vol. 46, no. 3, pp. 1455–1467, 2010.

[36] H. Ling, R.-C. Chou, and S.-W. Lee, "Shooting and bouncing rays: Calculating the RCS of an arbitarily shaped cavity," *IEEE Trans. Ant. Propagat.*, vol. 37, no. 2, pp. 194–205, 1989.

[37] M. Chen, C.-C. Chen, S. Y.-P. Chien, and R. Sherony, "Artificial skin for 76-77 ghz radar mannequins," *IEEE Transactions on Antennas and Propagation*, vol. 62, no. 11, pp. 5671–5679, 2014.

[38] G. Williams, "Overdetermined systems of linear equations," *The American Mathematical Monthly*, vol. 97, no. 6, pp. 511–513, 1990.

[39] M. Schepers, M. Giuberti, and G. Bellusci, "Xsens mvn: Consistent tracking of human motion using inertial sensing," 03 2018.

[40] INRAS, "Radarlog product description," http://www.inras.at/en/products/new-radarlog.html.

[41] P. Held, D. Steinhauser, A. Kamann, T. Holdgrün, I. Doric, A. Koch, and T. Brandmeier, "Radar-based analysis of pedestrian micro-doppler signatures using motion capture sensors," in *2018 IEEE Intelligent Vehicles Symposium (IV)*. IEEE, 2018, pp. 787–793.

[42] J. Wenger, "Automotive radar-status and perspectives," in *IEEE Compound Semiconductor Integrated Circuit Symposium, 2005. CSIC'05*. IEEE, 2005, pp. 4–pp.

[43] N. Yamada, Y. Tanaka, and K. Nishikawa, "Radar cross section for pedestrian in 76ghz band," in *Microwave Conference, 2005 European*, vol. 2. IEEE, 2005, pp. 4–pp.

[44] A. K. Ludloff, *Praxiswissen Radar und Radarsignalverarbeitung*. Springer-Verlag, 2013.

[45] Z. Wang, A. C. Bovik, H. R. Sheikh, E. P. Simoncelli *et al.*, "Image quality assessment: from error visibility to structural similarity," *IEEE transactions on image processing*, vol. 13, no. 4, pp. 600–612, 2004.

[46] S. M. Rubin and T. Whitted, "A 3-dimensional representation for fast rendering of complex scenes," in *ACM SIGGRAPH Computer Graphics*, vol. 14, no. 3. ACM, 1980, pp. 110–116.

[47] A. Fujimoto and K. Iwata, "Accelerated ray tracing," in *Computer Graphics*. Springer, 1985, pp. 41–65.